THE JOURNAL OF PHYSICAL CHEMISTRY C
A JOURNAL OF THE AMERICAN CHEMICAL SOCIETY

pubs.acs.org/JPCC

Article

Near-Infrared Chiral Plasmonic Microwires through Precision Assembly of Gold Nanorods on Soft Biotemplates

Amrita Chakraborty, Nonappa, Biswajit Mondal, Kamalesh Chaudhari, Heikki Rekola, Ville Hynninen, Mauri A. Kostiainen,* Robin H. A. Ras,* and Thalappil Pradeep*

Cite This: *J. Phys. Chem. C* 2021, 125, 3256–3267

Read Online

ACCESS | Metrics & More | Article Recommendations | Supporting Information

ABSTRACT: Directing the assembly of plasmonic nanoparticles into chiral superstructures has diverse applications including, chiroptical sensing, nonlinear optics, and biomedicine. Though soft template-mediated assemblies of both spherical and nonspherical gold nanoparticles have made significant progress, most approaches require sophisticated chemical synthesis or advanced methodologies. Besides, reports of structurally precise chiral plasmonic assemblies beyond nanoscale are limited. Here, we propose an efficient yet simple strategy to grow such precision assemblies up to mesoscale, which is beneficial for a broader community. Briefly, cationic gold nanorods (AuNRs) are allowed to systematically assemble along atomically precise, chiral, rodlike tobacco mosaic virus (TMV) particles via electrostatic attraction under ambient condition. This leads to spontaneous formation of helical hybrid microwires with high structural precision, as evidenced by cryogenic transmission electron microscopy and tomography. Resulting composite superstructures show a strong circular dichroism response at the plasmon wavelength of the AuNRs, which is supported by simulations using discrete dipole approximation. Further, chirality of the system is investigated at a single-microwire level using polarized dark-field scattering microscopy. An alternative chiral template, negatively charged colloidal cellulose nanocrystals, also arrange AuNRs into similar chiral microstructures. Thus, our report proposes a generic methodology to obtain chiral plasmonic response at the NIR region using inexpensive templates that will encourage the exploration of a wider range of nanoscale templates for creating hybrid mesostructures with emerging optoelectronic properties.

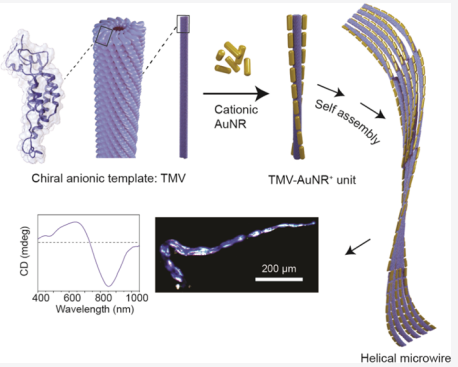

INTRODUCTION

Chirality is ubiquitous in nature and encountered at all length scales, from molecular-level to macroscopic objects. At molecular and macromolecular levels, biomolecules such as amino acids (except glycine), carbohydrates, proteins, and nucleic acids represent inherently chiral entities.[1] Further, at higher length scales, proteins (e.g., collagen and fibrin) and other biopolymers (e.g., agarose) undergo polymerization, resulting in helical fibrillar nanostructures.[2] Importantly, chiral entities absorb either right or left circularly polarized light preferentially (chiroptical properties). The differential absorption of right and left circularly polarized light leads to circular dichroism (CD).[3] CD spectroscopy is a powerful tool detecting molecular chirality,[4] protein folding−unfolding mechanisms, and conformational changes during chemical reactions.[5] However, most chiral organic molecules absorb in the ultraviolet (UV) region, and signals are weak in the visible region of the electromagnetic spectrum. Selective functionalization of dye molecules with chiral substituents allows CD signals in the visible range of the spectrum.[6] Beyond the molecular level, chirality can also be amplified using self-assemblies to achieve helices, twisted tapes, or twisted ribbon-like nanostructures.[7]

Unlike organic molecules, metal nanoparticles possess the capacity to confine light, enhancing light−matter interaction. Many theoretical[8,9] and experimental[10,11] studies have shown that incorporation of plasmonic nanoparticles dramatically enhances the chiroptical response of a chiral system, thereby lowering its detection limit. They also serve as building blocks for optical metamaterials. Moreover, these plasmon-enhanced CD signals shift to the position of the plasmon resonance frequency of the respective nanoparticles, i.e., the visible−near-infrared (NIR) region.[12,13] Thus, a broad wavelength range can be exploited simply by regulating the size and shapes of the nanoparticles. Such a phenomenon has application potential in circular polarizers,[14] detectors of circularly polarized light,[15] sensors of biomolecules,[16] and asymmetric catalysis.[17] Therefore, strategies to efficiently conjugate plasmonic property and chirality have become an active field of research. Nanostruc-

Received: December 27, 2020
Revised: January 8, 2021
Published: February 1, 2021

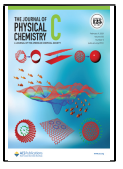

https://dx.doi.org/10.1021/acs.jpcc.0c11512
J. Phys. Chem. C 2021, 125, 3256–3267

tures with right- or left-handedness in their intrinsic morphology give highly intense CD signals. But they are either fabricated by a top-down approach like nanolithography, which has limitations in producing genuinely three-dimensional morphologies, especially in large-scale production, or achieved through wet chemical syntheses that are laborious, complex, and suffer from nonuniformity and poor reproducibility.

Therefore, functionalization of commonly available spherical or anisotropic noble-metal nanoparticles (NMNPs) with chiral moieties such as cysteine,[18] peptides,[19] polyfluorenes,[10] or DNA,[20] has evolved as a rather straightforward approach to induce chirality. Due to the interaction between these chiral molecules and the plasmon of the achiral nanoparticle, such composites show a prominent CD signal, which is called surface plasmon-enhanced circular dichroism (SPECD). From the numerous theoretical[8,21,22] and experimental studies[18,19,23] we can conclude that SPECD produces the strongest signal when chiral molecules are placed at the plasmonic hotspots within a 3D nanoparticle assembly. However, placing a single molecule in the hotspot with precision is challenging. Govorov and co-workers have shown that spherical gold nanoparticles, arranged in an asymmetric, i.e., tetrahedral or helical geometry, produce a collective CD signal at their plasmonic resonance frequency.[21] Since then, a number of methodologies have been developed to arrange presynthesized NPs of desired size and shape along a soft helical backbone, e.g., peptides,[24,25] nematic liquid crystals,[26] fiber-like soft materials,[27] supramolecular backbones,[28] and DNA origami.[29,30] The success of this strategy lies in the extent of precision by which the template can regulate the nanoparticles' three-dimensional arrangement. DNA origami, being programmable, serves as one of the precise methods for arranging NMNPs in a desired geometry.[31] However, the cost-intensive nature and high level of expertise required for DNA nanotechnology prohibit it from being the most accessible strategy for materials scientists. Thus, although the field of template-assisted chiral plasmonic nanomaterials has made considerable progress, there is still room for a strategically simple way to assemble metallic nanoparticles on inexpensive soft templates with high structural precision. Bacterial cells[32] and viral capsids of well-defined structures[33] are recently being explored as alternative building blocks of higher-level assemblies, leading to functional nanomaterials. Simple electrostatic interactions can efficiently assemble protein cages within themselves,[34] as well as with plasmonic nanoparticles,[35] creating highly ordered superstructures. Keeping these in mind, we have chosen tobacco mosaic virus (TMV) as the chiral template. Native TMV is a biocolloidal substrate of rodlike morphology with known crystal structure, highly negative surface charge (ζ-potential, −25.4 mV in phosphate buffer of pH 7.8), and precise size and shape monodispersity. A viral RNA, helically wrapped by 2130 coat proteins, generates a right-handed chirality in its structure.[36] In the present work, we have allowed cationic AuNRs to arrange along the TMV surfaces through electrostatic self-assembly and observed a strong bisignate circular dichroism signal at the visible−NIR wavelength range. The generality of our strategy to create NIR chiral plasmonic microwires is established using cellulose nanocrystals (CNC) as another template. DNA origami and peptide production technologies, though result in assemblies of high structural precision, are not easily scalable. On the contrary, extraction and purification procedures of TMVs and CNCs are well established in plant biotechnology, allowing the production of these templates in kilograms. Moreover, for various device-based applications like telecommunication, significant effort has been made to make mesoscale helical superstructures.[37] The morphology and surface charge distribution of TMV and CNC guide a spontaneous translation of chirality from nanoscale to micron scale range, which is a clear advantage of the present strategy. Thus, our approach addresses some of the most important challenges of achieving precision assembly of nanoparticles up to micron scale toward creating SPECD in the NIR region.

EXPERIMENTAL METHODS

Preparation and Characterization of Tobacco Mosaic Virus Particles. The leaves of a month-old *Nicotiana tabacum* (var. Samson) plants were inoculated by rubbing them with wild-type TMV stock. The upper leaves that showed severe TMV symptoms were collected after 22 days to achieve 52 g of leaf biomass. TMV was purified following the procedure reported by Chapman.[38] Precisely, 0.5 M phosphate buffer of pH 7.2 along with 1% (v/v) 2-mercaptoethanol were used to homogenize the leaves. The leaf juice was filtered and extracted with butan-1-ol, centrifuged, and the aqueous phase was collected. PEG 8000 (4%) was used to precipitate the TMV. This pellet of virus was washed by phosphate buffer (10 mM, pH 7.2) mixed with 0.7 M NaCl and 4% PEG. It was then resuspended and further purified according to Liljeström et al.[39] The stock TMV was diluted using DI water just before the experiments.

Synthesis of AuNR. Highly monodisperse gold nanorods of aspect ratio ∼3.4 were prepared following a seedless synthetic procedure proposed by our group.[40] CTAB solution (20 mL, 100 mM) was taken in a 50 mL conical flask and kept in a water bath to maintain the temperature at 28 °C. To this, 1 mL of 10 mM $HAuCl_4{\cdot}3H_2O$, 130 μL of 10 mM freshly prepared $AgNO_3$, and 140 μL of 100 mM fresh ascorbic acid were added sequentially with mild stirring. As soon as the brownish-yellow solution (due to the complex formed by CTAB and $HAuCl_4$) became colorless due to the reduction of Au^{3+} to Au^{+} by ascorbic acid, 200 μL of 1.67 mM $NaBH_4$ (freshly prepared in ice-cold water) was added at one shot. The stirring was stopped immediately after the addition of $NaBH_4$. Although the colorless solution slowly turned dark brown within 30 min, showing the high yield of nanorods, it was kept undisturbed for at least 4 h to ensure that the growth was complete.

Cationization of AuNRs. The excess CTAB-stabilized AuNRs were washed using distilled water for further use. For that, the as-synthesized AuNRs were taken in 2 mL plastic vials and centrifuged at 13 000 rpm for 20 min, the supernatant from each vial was discarded, and the precipitate was resuspended in 1.5 mL of DI water. This was again centrifuged in a similar way, but this time, the precipitate was not resuspended in water. Rather, 20 μL of 4 mM ethanolic solution of (11-mercaptoundecyl)-*N*,*N*,*N*-trimethylammonium bromide (MUTAB) was added to the pellet in each vial and shaken vigorously for 30 min. It was kept overnight without stirring and then washed with water. Precisely, the pellet was dispersed in 2 mL of DI water, centrifuged, and then 1.9 mL of water was decanted. Finally, it was dispersed in a suitable amount of water to attain an absorbance of 1.2 such that the MUTAB concentration in the solution was significantly less than 0.002 mM.

https://dx.doi.org/10.1021/acs.jpcc.0c11512
J. Phys. Chem. C 2021, 125, 3256−3267

Synthesis of CNCs. As described by Hynninen et al.,[41] Whatman grade 1 filter papers were ground to form a homogeneous powder. To 15 g of this paper powder, 64% sulfuric acid solution was added in a round-bottom flask and mixed thoroughly by stirring. This was hydrolyzed at 45 °C for 45 min and then diluted 10 times using Milli-Q water to cease the reaction. This was kept still until complete sedimentation. The precipitate was collected after decanting the clear supernatant. The pellet was redispersed in Milli-Q water and centrifuged at 6000 rpm for 20 min first, and in the second round, at 2500 rpm for 45 min. Further purification was carried out by dialysis against Milli-Q water until the conductivity of the dialysate reduced below 5 μS/cm. Then, it was passed through a Whatman 541 filter paper and stored at +4 °C. The concentration of CNC was determined gravimetrically by slow evaporation of water and the stock solution was found to be 3.5 wt %.

TMV-AuNR$^+$ Assembly Formation. The MUTAB-functionalized AuNR$^+$ solution was diluted by adding DI water until the absorbance of the LSPR was ∼1.2. The TMV stock solution was diluted using DI water to 0.21 mg/mL. The diluted TMV solution was added at 25 μL steps to a cuvette for UV−vis spectrometer, containing 2 mL of AuNR$^+$ solution and mixed gently using a pipette. After every addition, absorption spectra were measured to ensure systematic assembly from the slight gradual shift in the absorption peak maxima. There was no significant time gap needed between TMV addition and measurement of absorption spectra.

CNC-AuNR$^+$ Assembly Formation. This was the same as the assembly with TMV. CNC of 0.009 mg/mL concentration was added in 2 μL steps.

Instrumentation. All of the UV−vis absorption spectra were recorded using a PerkinElmer Lambda 25 UV−vis spectrometer.

The TEM measurements were performed using a JEOL 3010 (JEOL Japan) transmission electron microscope, using a 200 kV acceleration voltage.

SerialEM and 3D Reconstruction. For transmission electron tomographic reconstruction, tilt series of 2D projections were acquired with the SerialEM software package.[42,43] The specimen was tilted between ±69° angles with 2° increment steps under low-dose mode.[44] The acquired stack of images was first subjected to a series of preprocessing, coarse alignment, and final alignment, and further aligned using IMOD software package.[45] The final aligned file was then utilized for 3D reconstruction with custom-made maximum entropy method (MEM) program with a regularization parameter value of $\lambda = 1.0 \times 10^{-3}$ on MacPro.[46] The 3D isosurface and solid colored images were produced using UCSF Chimera.

Cryo-Transmission Electron Microscopy. The cryo-TEM images were collected using a JEM 3200FSC field emission microscope (JEOL) operated at 300 kV in bright-field mode with an Omega-type zero-loss energy filter. Prior to sample preparation, 200-mesh copper grids with a lacey carbon support film (Electron Microscopy Sciences) were plasma-cleaned using a Gatan Solarus (Model 950) plasma cleaner for 30 s. The samples for Cryo-TEM imaging were prepared by placing 3 μL of the sample on plasma-treated TEM grids and plunge-frozen into a −170 °C ethane−propane (1:1) mixture using a Leica automatic plunge freezer EM GP2 with 2 s blotting time under 100% humidity. The vitrified specimen was cryo-transferred to the microscope. The images were acquired with Gatan Digital Micrograph software, while the specimen temperature was maintained at −187 °C.

Circular Dichroism Study. The circular dichroism spectra of all of the samples were measured in a Jasco J-1500 spectrometer. A quartz cuvette of 10 mm path length was used for each measurement.

Modeling the Circular Dichroism. We used discrete dipole approximation (DDA)[47,48] to calculate the CD signal for a nanoparticle assembly. The nanoparticle coordinates were determined from TEM tomography measurement, and the model contained 293 nanoparticles. The exact orientation of the nanorods could not be extracted from the tomography data; instead, we had set the long axis of the nanorods along the main axis of the nanorod assembly with a normally distributed variance (sigma) of 20°. The length of the nanorod was set to 34 nm with a variance of 6.2 nm, and the diameter was set to 10 nm with a 2 nm variance. As the parameters had a randomly generated component, all of the results presented were average values obtained from 40 simulation runs.

In the simulations, each nanoparticle was represented by a point dipole. The polarizability of the point dipole was calculated using the modified long-wavelength approximation (MLWA),[49] assuming an ellipsoidal shape for the particle

$$\alpha_{\mathrm{MLWA},j} = \frac{\alpha_j}{1 - \frac{k^2}{j}\alpha_j - \frac{2}{3}ik^3\alpha_j}$$

where α_j is the quasistatic polarizability of the particle along its semiaxes $j = [a, b, c]$, given by

$$\alpha_j = 4\pi abc\frac{\varepsilon_1(\omega) - \varepsilon_2}{3\varepsilon_2 + 3L_j(\varepsilon_1(\omega) - \varepsilon_2)}$$

The term L_j is given by[50]

$$L_j = \frac{abc}{2}\int_0^\infty \frac{dq}{(q + j^2)\sqrt{(q + a^2)(q + b^2)(q + c^2)}}$$

Finally, the polarizability of the nth nanoparticle of the structure is represented by a matrix

$$\alpha_n = \begin{pmatrix} \alpha_{\mathrm{MLWA},a} & 0 & 0 \\ 0 & \alpha_{\mathrm{MLWA},b} & 0 \\ 0 & 0 & \alpha_{\mathrm{MLWA},c} \end{pmatrix}$$

This polarizability matrix was then rotated for each nanoparticle to account for the different orientations of the nanorods within the structure. Finally, we calculated the CD response of the self-assembled system using the discrete dipole approximation (DDA).[47,48] The induced dipole moments in the whole nanoparticle assembly were

$$\mathbf{P} = (1 - \hat{\boldsymbol{\alpha}}\,\mathbf{G}^0)^{-1}\hat{\boldsymbol{\alpha}}\,\mathbf{E}^{\mathrm{ext}}$$

We calculated the matrix inversion and used it to evaluate the dipole moments for different incident fields $\mathbf{E}_{\mathrm{ext}} = \mathbf{E}_k^{\mathrm{L/R}}\exp(i\mathbf{k}\cdot\mathbf{r})$. Here, the vector $\mathbf{k}$ was scanned over 100 different orientations on a unit sphere to obtain an average response of the structure to match the experiment done in solution, and $\mathbf{E}_k^{\mathrm{L/R}}$ defines the left- and right-handed polarizations for the corresponding $\mathbf{k}$-value. From the dipole moments, we calculated the extinction cross section as

https://dx.doi.org/10.1021/acs.jpcc.0c11512
J. Phys. Chem. C 2021, 125, 3256−3267

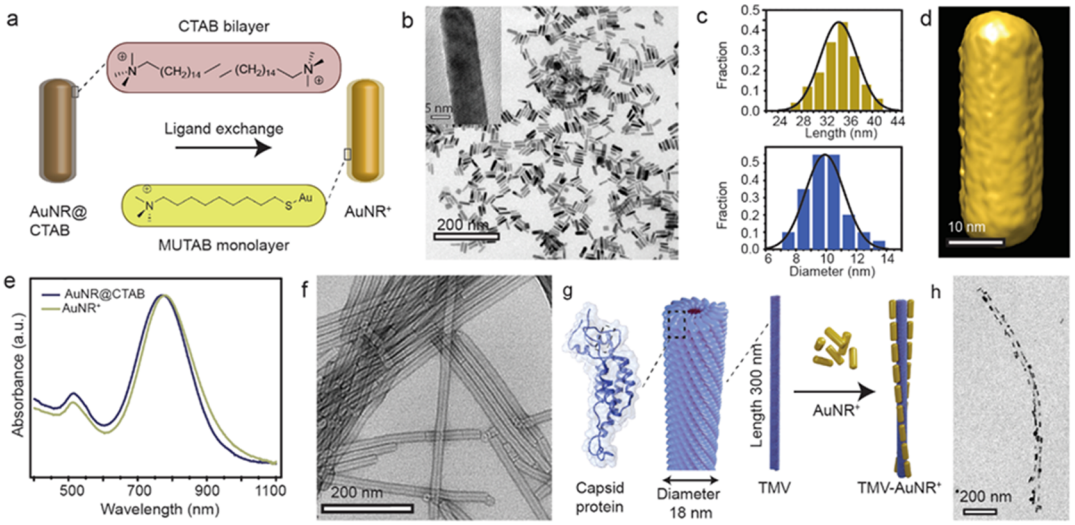

Figure 1. Starting materials and product of the electrostatic assembly. (a) Schematic of the functionalization of AuNR@CTAB with MUTAB via ligand exchange method, (b) TEM image of AuNR$^+$, (c) distribution of length and diameter of 200 AuNR$^+$s measured from the TEM images, and (d) TEM tomographic image of a single AuNR$^+$. (e) Comparative absorption spectra of AuNRs before and after MUTAB functionalization. (f) TEM image of negatively stained TMVs. (g) Cartoon representation of the TMV structure and the schematic presentation of the electrostatic interaction between TMV and AuNR$^+$. (h) TEM image of the resulting TMV-AuNR$^+$ composite.

$$\sigma_{ext} = 4\pi k \sum_{j=1}^{N} \frac{\mathrm{Im}[\mathbf{E}^*_{ext,j} \cdot \mathbf{p}_j]}{|E_{ext,j}|^2}$$

and the absorption cross section as[47]

$$\sigma_{abs} = 4\pi k \sum_{j=1}^{N} \frac{1}{|\mathbf{E}_{ext,j}|^2} \left\{ \mathrm{Im}\left[\mathbf{P}_j (\alpha_j^{-1})^* \mathbf{P}_j^* - \frac{2}{3} k^3 |\mathbf{P}_j|^2 \right] \right\}$$

Finally, the circular dichroism signal was calculated from the cross sections as

$$\frac{\sqrt{\sigma_R} - \sqrt{\sigma_L}}{\sqrt{\sigma_R} + \sqrt{\sigma_L}}$$

Here, the subindices R and L corresponded to the two different circular polarizations.

RESULTS AND DISCUSSION

Cationization of AuNRs. Spherical nanoparticles of gold typically generate CD signals of moderate intensity over a narrow spectral range.[13,24] On the contrary, AuNRs are capable of generating a much stronger electronic field owing to the anisotropic distribution of their free electrons.[31] Besides, their longitudinal surface plasmon resonance (SPR) frequency is highly sensitive to their size, aspect ratio, and electronic environment, i.e., the presence and orientation of neighboring particles. Hence, AuNRs are promising building blocks for tunable and intense CD signal. In an aqueous medium, cetyl trimethylammonium bromide (CTAB) molecules form a bilayer that covers the AuNRs. Although the ζ-potential of CTAB-protected AuNR (AuNR@CTAB) is highly positive (+30 mV) due to the quaternary amine group of CTAB, there is no covalent bond between the gold atoms and the CTAB molecules, making the protective layer labile. Therefore, using a typical ligand exchange method, we functionalized the AuNRs with a thiol, containing positively charged end group and a chain length comparable to that of CTAB, namely, (11-mercaptoundecyl)-*N*,*N*,*N*-trimethylammonium bromide (MUTAB). The Au−S bond formation facilitated the replacement of CTAB bilayer by MUTAB molecules, producing MUTAB-protected AuNRs, which is abbreviated here as AuNR$^+$ (Figures 1a and S1). The TEM image of AuNR$^+$ (Figure 1b) and the distribution of their length and diameter (Figure 1c) suggest uniform shape and narrow size dispersity, with the mean length being 34 ± 4.5 nm and mean diameter being 10 ± 1.2 nm (aspect ratio, ∼3.4). The 3D reconstruction of a single AuNR$^+$ morphology using electron tomography is shown in Figure 1d and Video S1. Its comparison with that of AuNR@CTAB (Figure S2) further shows that the morphology was intact on ligand exchange. Comparing the absorption spectra of AuNR@CTAB and AuNR$^+$ (Figure 1e), it can be concluded that the ligand exchange did not alter the dispersity and electronic environment of the as-synthesized AuNRs. The resulting AuNR$^+$ retained its cationic nature, as suggested by its positive ζ-potential (+18 mV).

Assembly of AuNR$^+$ on TMV. TMV is an anisotropic biocolloidal substrate with a radius of 18 nm and a length of 300 nm (Figure 1f).[36] The virus is semiflexible, atomically precise, and therefore highly suitable as a soft template for drug delivery,[51] ordered assemblies of chromophores,[52] nanoparticles,[53] and deposition of metal ions.[54] The crystal structure of TMV reveals that there are 130 turns of the coat proteins along the length of a single TMV causing a spiral negative charge distribution on the surface.[55] Therefore, cationic AuNR$^+$ got adhered on the TMV guided by the strong electrostatic attraction. In case of such assemblies, the relative position of adjacent nanoparticles has great influence on the final structure and properties of composite materials. Moreover, nanorods being anisotropic in morphology, the relative angles between the longitudinal axes of AuNR$^+$s within themselves and between AuNR$^+$s and TMVs act as another crucial parameter while forming a binary assembly. Previously, it has been observed that AuNRs have a tendency to follow the orientation of anisotropic templates.[56] In this case also, directional synergy played an important role, which led the AuNR$^+$s to attach to the TMV particles keeping their longitudinal axis almost parallel to that of the TMV. This

https://dx.doi.org/10.1021/acs.jpcc.0c11512
J. Phys. Chem. C 2021, 125, 3256−3267

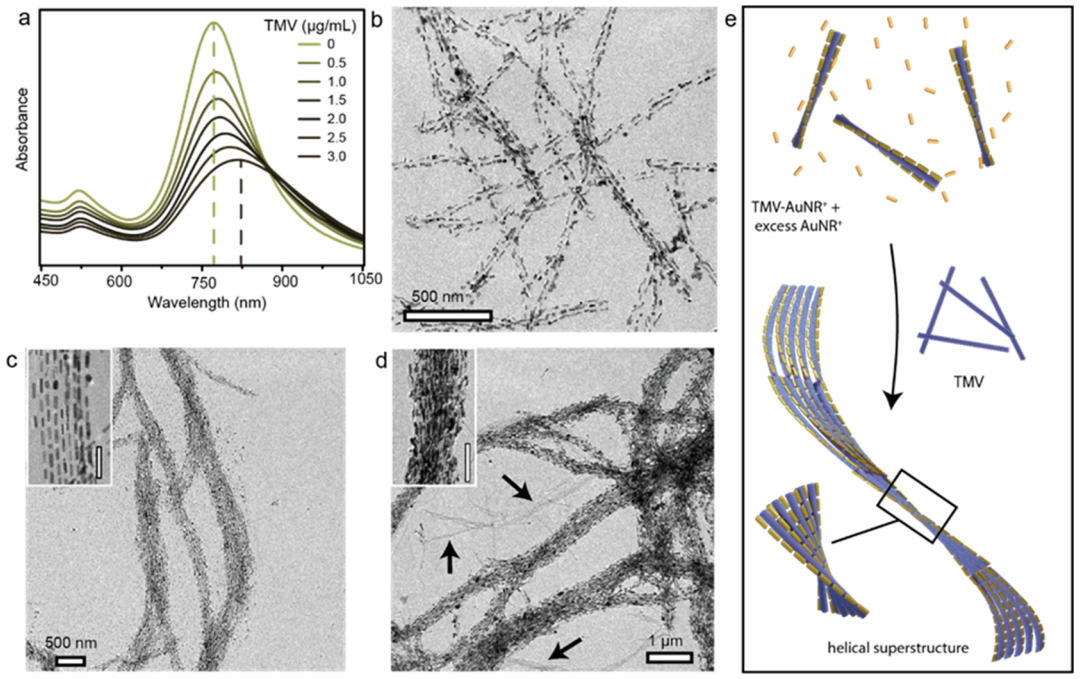

Figure 2. Long-range assembly of TMV-AuNR$^+$s. (a) Change in the absorption spectra of AuNR$^+$ (0.16 nM) with gradual TMV addition. (b) TEM image of the assembly at 2 μg/mL TMV. (c) TEM image of the assembly at 6 μg/mL TMV showing ribbon-like morphology; the magnified image in the inset reveals its 2D superlattice (scale bar, 50 nm). (d) TEM image of a bundle-like assembly at 10 μg/mL TMV; the magnified image in the inset shows 3D superlattice (scale bar, 500 nm), and the arrows point to the excess TMVs. (e) Schematic of the assembly formation.

structure was also favored by the maximum attraction between cationic AuNR$^+$ and anionic TMVs. Figure 1g represents the electrostatic assembly schematically, and Figure 1h shows a TEM image of the resulting TMV-AuNR$^+$ composite. Notably, the AuNR$^+$ aligned themselves in stripes on opposite sides of the cylindrical TMV rather than covering their entire surface evenly, as observed previously by Liz Marzan's group in the case of carbon nanotube template.[57] The perfectly cylindrical shape of TMV led to the end-to-end arrangement of AuNR$^+$s without any defect (misalignment of rods) enabling greater uniaxial plasmon coupling.

Long-Range Assembly of TMV-AuNR$^+$. TMVs are well dispersed in the aqueous medium, owing to their high negative surface charge. However, they are known to form 2D hexagonally close-packed bundles under certain conditions.[58,59] Stoichiometric ratio of the two constituents is crucial for a binary assembly. Hence, to study the assembly at different stoichiometric ratios of AuNR$^+$ and TMV, the latter was added stepwise to 0.16 nM AuNR$^+$ solution and analyzed after each addition. The volume of TMV solution was too small (final dilution was 5%) to significantly alter the AuNR$^+$ concentration in the medium. Figure 2a shows the change in the absorption spectrum of AuNR$^+$ during the process. The longitudinal surface plasmon resonance (LSPR) band of AuNR$^+$, i.e., the one appearing at the longer wavelength (here at ~770 nm), is known to be more sensitive to any change in the system compared to the transverse surface plasmon resonance (TSPR) band at 520 nm. In agreement, we observed a gradual redshift of the LSPR peak maximum with increasing concentration of TMV along with a decrease in the value of absorbance, peak broadening, and rise in the baseline. The redshift implies plasmonic coupling among the AuNR$^+$s in the longitudinal direction. As a control experiment, a comparable concentration of MUTAB was added to native TMV, and their TEM image revealed that it did not induce any specific interaction among TMVs (Figure S3a). At a low TMV concentration, we observed that some of the AuNR$^+$ assembled along the TMVs and excess AuNR$^+$ was found to remain dispersed in the medium (Figure S3b). With an increase in the TMV concentration, increasingly more AuNR$^+$ took part in the binary assembly. The resulting LSPR peak broadened as it was now having contributions from both free AuNR$^+$ (LSPR at ~770 nm) and AuNR$^+$s arranged onto the TMV surfaces (LSPR at >770 nm). These two factors, together with the rise in the baseline, indicate the abundance of TMV-templated assembly of AuNR$^+$ to higher-order structures in the medium. Figure 2b–d shows the TEM images of the resulting composite structures in the presence of 2, 6, and 10 μg/mL TMV, respectively. The electron microscopy images suggest that as the concentration of TMV increases, the discrete TMV-AuNR$^+$ units containing one TMV each, acted as the nucleating sites and excess TMV and AuNR$^+$ participated in further assembly, leading to a long-range structure. Owing to the complementary hydrophobic interactions between the dipolar ends of the helical structure, TMVs are known to take part in a head-to tail assembly.[60] In accordance, initially, the TMV-AuNR$^+$ structures grew longitudinally much more than in the transverse direction, as shown in Figure 2b. Unidirectional assembly of native TMVs is favored as this minimizes the repulsion between the carboxylic residues at the assembly interface. But upon AuNR$^+$ attachment, the negative surface charge of TMVs was neutralized. Therefore, growth of the assembly in the transverse direction also became feasible. This process maximized the attractive force between the two components with opposite surface charges and minimized the repulsive force between similar surface charges. As shown in Figure 2c, gradually, it took the shape of a ribbon, showing an ABAB... arrangement along the width, where A = TMV and B

https://dx.doi.org/10.1021/acs.jpcc.0c11512
J. Phys. Chem. C 2021, 125, 3256−3267

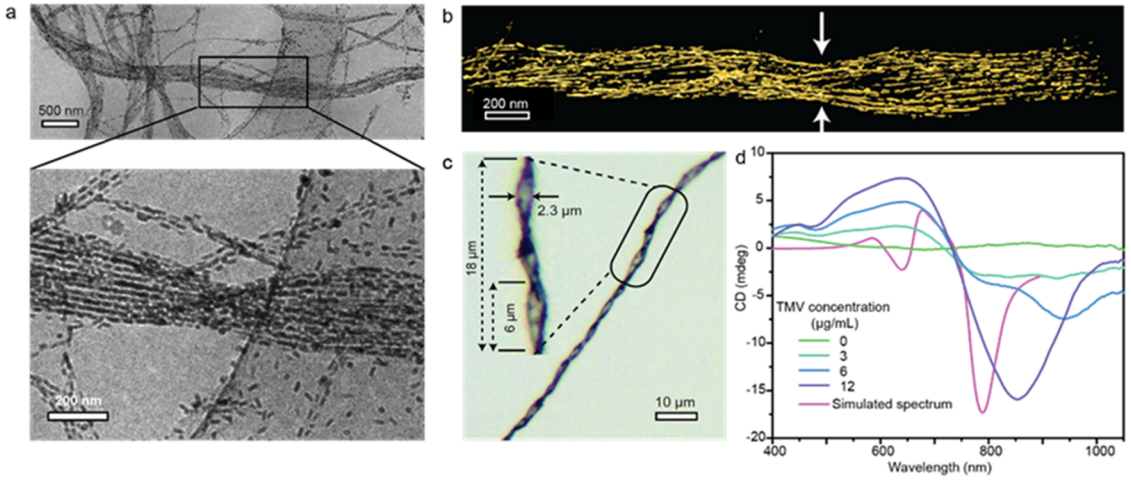

Figure 3. Plasmonic chirality of the TMV-AuNR$^+$ wires. (a) Cryo-TEM image of a ribbon-like TMV-AuNR$^+$ superstructure along with the magnified view of a twisted section and (b) the corresponding 3D reconstructed image with arrows pointing to the helical twist. (c) Optical image of a TMV-AuNR$^+$ microwire in the presence of 12 μg/mL TMV showing repetitive twists. Magnified view of the marked section shows the pitch length. (d) Experimental CD spectra showing stronger signals with gradually higher TMV concentration, along with the simulated CD spectrum calculated from the AuNR$^+$ coordinates obtained from (b).

= linear array of AuNR$^+$. The inset in Figure 2c presents a magnified view revealing the 2D superlattice domains of these superstructures. Figure 2e schematically presents the long-range assembly. With a further increase in the TMV concentration, due to overgrowth, this 2D ribbon-like superstructure attained thick wirelike morphology with 3D bundled superlattice structures (as shown in Figure 2d). Beyond this point, addition of TMV only made these wires thicker and longer without any significant morphological change. Finally, these wires with length of several microns started to precipitate and excess free TMV can be observed in the corresponding TEM images.

Origin of the Helical Structure Leading to Plasmonic Chirality. From Figure 2, it is evident that the long and thick TMV-AuNR$^+$ superstructures contain hints of structural twists in the long range. To eliminate any drying artifact, we characterized this binary superstructure under cryogenic conditions. Although the periodic array of TMVs and AuNR$^+$ appears parallel locally (inset in Figure 2c), the cryo-TEM image in Figure 3a shows that the ribbon-like TMV-AuNR$^+$ composite wires indeed show helicity in their structure. A magnified image displays that it is completely twisted at places. Using a tilt series of images, we reconstructed a 3D structure of this wire (Figure 3b, Video S2), which presents a clearer view. The origin of this helicity lies in the crystal structure of TMV, where a right-handed RNA helix is buried inside the capsomeres. These capsomeres show an axial repeat distance of 69 Å, which consists of 49 subunits, while the basic helix makes three turns. Previous studies have shown that chiral rod-shaped viruses align in a twisted manner with each other to minimize their interaction energy.[61] In this case, the net effect of a strong attraction between AuNR$^+$ and TMV and the helical distribution of negative charge along the TMV surface gave rise to the helicity in the superstructure. In a study by Liljeström et al.,[39] spherical cationic gold nanoparticles, in a high electrolyte concentration, were mixed with TMVs and the mixture was dialyzed. This way, instead of any kinetically driven random electrostatic assembly, the authors obtained a highly ordered ribbon-like superstructure through a zipper-like mechanism. Furthermore, the superstructure showed helicity, generating a CD signal around the plasmon wavelength of AuNPs. The success of this strategy lies in the colloidal stability of the AuNPs against the electrolyte. However, in some cases, the plasmonic nanoparticles tend to aggregate irreversibly even at a moderate salt concentration. The present study addresses this limitation. We show that fairly ordered helical superstructures can be achieved by a slow stepwise addition of the chiral template to the pool of AuNR$^+$, without the risk of electrolyte treatment. We also note that the helicity became more prominent with the growth of the superstructure. Figure 3c presents an optical microscopy image of a composite ribbon-like structure that is several hundreds of microns in length and up to 2.3 μm in width. Periodic structural twists can be seen along the entire microwire. The inset shows a magnified view of the marked portion, which reveals a pitch of 6 μm. The optical images of the system at various TMV concentrations in Figure S4 show that at a lower TMV concentration, the structures contained occasional twists. However, at TMV concentrations higher than 12 μg/mL, the pitch increased with the width of the microwires (Figure S4b,c). Thus, through the self-assembly process, the molecular-level chirality was transposed to the chiral structures of multiple orders of magnitude larger length scales. Notably, in the proposed mixing protocol, we hypothesize that each structural unit of the template got saturated by AuNR$^+$ before more templates entered the system. However, when we performed the reverse addition process, i.e., gradually added a small amount of AuNR$^+$ to an aqueous solution of TMV, the former chose random structural units of TMV to attach to. This continued, making the subsequent long-range assembly impossible. In the cryo-TEM images, we see that the assembly did not continue beyond a few TMV-AuNR$^+$ units (Figure S5).

Besides, the circular dichroism measurements reveal that the structural helicity of the microwires had a preferred handedness that gave rise to an overall chirality. In Figure 3d, we see that the system gives a bisignated CD signal of peak-dip feature with a zero-crossing point around the absorption maximum of the AuNR$^+$. This nature of the CD spectra is typical for helical plasmonic assemblies. Here, although the AuNR$^+$s arranged on

https://dx.doi.org/10.1021/acs.jpcc.0c11512
J. Phys. Chem. C 2021, 125, 3256−3267

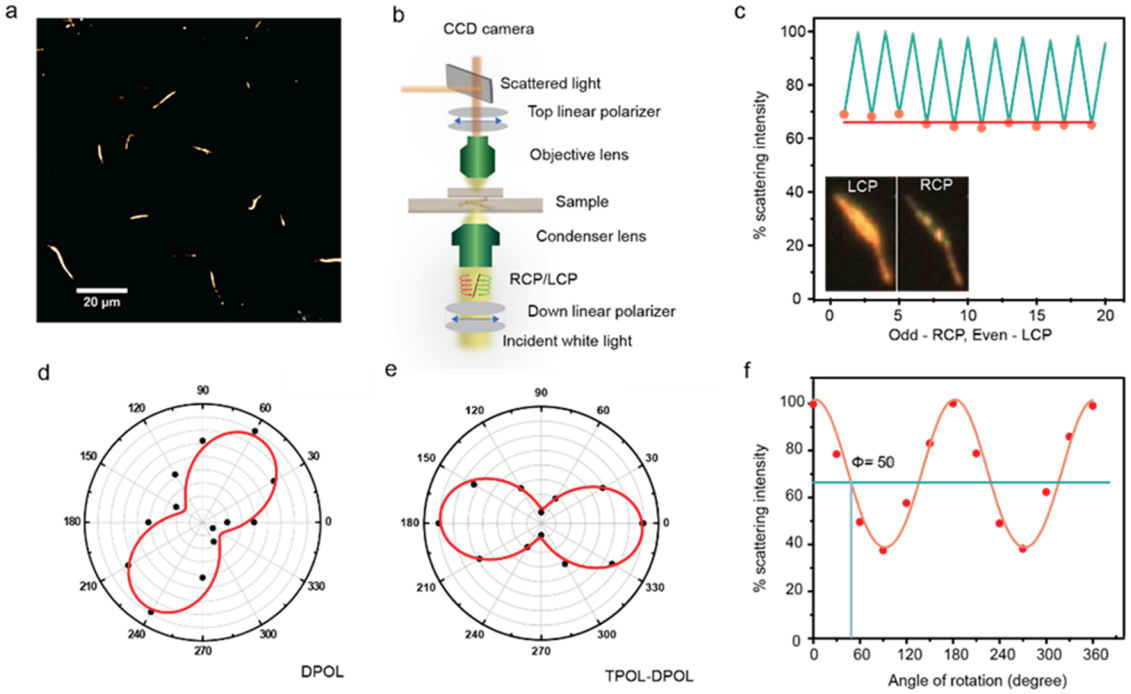

Figure 4. Chirality study of single microwires. (a) Dark-field optical image of the composite wires made of TMV-AuNR$^+$, (b) schematic representation of the PDFSMS setup, and (c) changes in the scattering intensity of a single microwire (the inset shows the images) when it was illuminated with RCP and LCP alternatively and observed through an analyzer. (d) Polar map of a single wire when it was illuminated with a linearly polarized light at different angles (0−360°) without analyzer and (e) with analyzer. (f) The polar plot in (e) presented as a 2D *XY* plot to find the angle of optical rotation of a microwire.

the surface of TMV in near-parallel 1D arrays, the right-handed distribution of surface charge on TMV guided the assembly to finally give the right-handed global twists. As explained in detail in the previous study with gold nanoparticles by Liljeström et al.,[39] if one observes from the transverse direction, the nanorods show a left-handed arrangement, which gives the peak-dip-type CD signal. In solution, the experimental CD spectra are the average of chiral signals coming from the axial as well as transverse directions of the TMV-AuNR$^+$ composite microwires. Now, considering the micron-scale length of the wires, any light propagating along their longitudinal axis would be heavily damped by the gold nanorods, decreasing the contribution of this orientation in the experimental CD. Therefore, the left-handed arrangement from the transverse direction predominates and the resulting signal follows the peak-dip nature. A similar CD signal was also reported by Nicholas A. Kotov's group for ribbon-like chiral plasmonic composite structures.[62]

As predicted from the electron microscopy and optical images, with a higher TMV concentration in the medium, the CD signal became stronger in both positive and negative sides while keeping the baseline and the zero-crossing position almost constant. Beyond a certain TMV concentration (12 μg/mL of TMV), as the wires became too heavy to stay dispersed in the aqueous medium, the bulk CD spectrum got flattened (Figure S6). To avoid dependency of chirality on concentration, asymmetry factor or *g*-factor of the system was calculated from these CD spectra and the corresponding absorbance spectra at different TMV concentrations following an established method.[63] As shown in Figure S6c, a prominent peak-dip trend of the spectrum was observed for 12 μg/mL TMV concentration that shows a standard value for this kind of systems.[62] Using the CD data and corresponding absorbance values from Liljeström et al.,[61] the *g*-factor of TMV-gold nanoparticle system at a 200 mM salt concentration is also plotted in Figure S6d. Both the systems show comparable negative peak intensity, but a much stronger (∼10 times higher) positive signal in the case of TMV-AuNR$^+$ suggests better chiral response in the case of AuNR$^+$. Taking the position of the AuNR$^+$s in the assembly from the coordinates of its cryo-TEM tomogram and using the discrete dipole approximation (DDA), we simulated the CD signal of the TMV-AuNR$^+$ microstructure shown in Figure 3b. The model contains 293 nanorods, each represented as a point dipole, with polarizability obtained from the modified long-wavelength approximation (MLWA). Taking the length of the nanorods as 34 ± 6 nm and the diameter as 10 ± 2 nm (for details, see the Experimental Methods section), we obtain the CD spectrum presented along with the experimental spectra in Figure 3d. The zero-crossing position of this simulated spectrum matches well with our experimental result, the signal intensity being comparable to the one when the TMV concentration was 12 μg/mL. The sharpness of the simulated CD spectrum can be attributed to the fact that the model takes coordinates from the cryo-tomographic image of a single structure. However, in solution (as shown in Figure 3a), the length and width of the microwires vary to some extent, which contribute to the broadening of bulk CD spectra. The experimental spectra are smoothened and the simulated spectrum is multiplied by a simple integer for ease of comparison.

Chirality Estimation at Single-Microwire Level. Owing to its ensemble-averaging nature, bulk CD measurements often mask the sensitivity of CD spectroscopy. Therefore, researchers are having a growing interest in detecting chirality at a single-particle level using far-field extinction microscopy[64]

https://dx.doi.org/10.1021/acs.jpcc.0c11512
J. Phys. Chem. C 2021, 125, 3256−3267

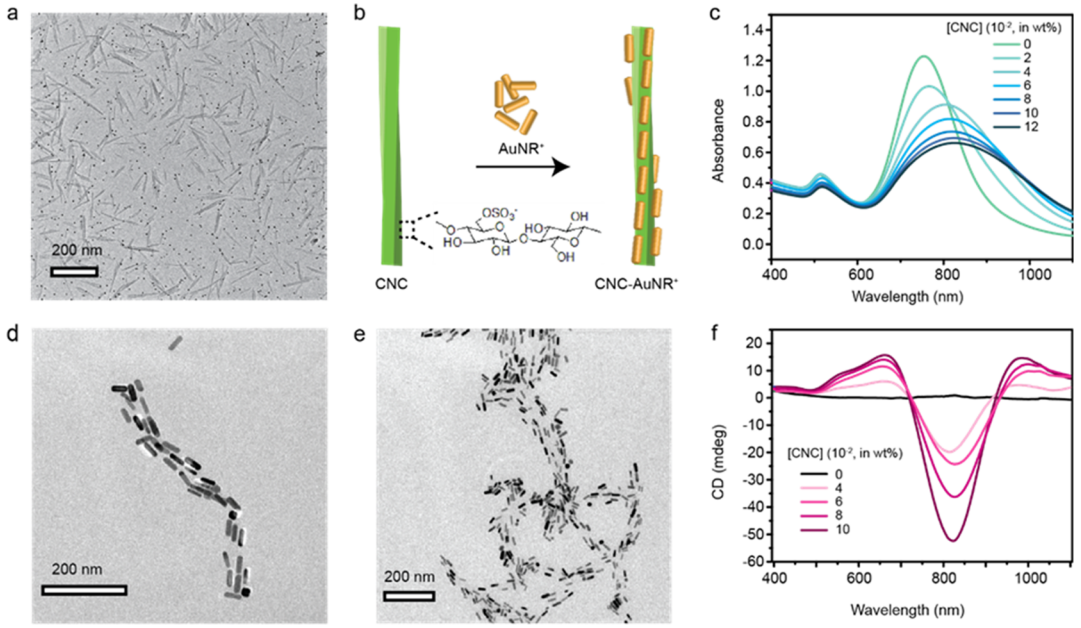

Figure 5. Long-range assembly of AuNR$^+$ with CNC. (a) Cryo-TEM image of negatively stained CNCs, (b) schematic of the arrangement of AuNR$^+$ on twisted CNC surface, (c) change in the absorption spectrum of AuNR$^+$ with gradual addition of CNC. TEM images of (d) short-range assembly at 0.02 wt % of CNC and (e) long-range assembly at high CNC concentration (~0.06 wt %). (f) CD spectra of the sample with increasing CNC concentrations.

and single-particle chiral scatterometry.[65] Using a much simpler technique, namely, polarized dark-field scattering microspectroscopy (PDFSMS), we have determined the chirality associated with individual composite TMV-AuNR$^+$ microwires. PDFSMS allows the detection of chirality associated with individual gold nanorod aggregates both qualitatively and quantitatively.[66] This is possible because of the optical rotation due to plasmonic circular dichroism of the anisotropic nanoparticle assemblies. Here, using the same principle and experimental setup, we studied chirality associated with individual TMV-AuNR$^+$ microwires. Precisely, we used an upright dark-field microscope to image the TMV-AuNR$^+$ sample placed between a glass slide and a glass coverslip. Depending on the TMV-to-AuNR$^+$ ratio, we observed dotlike, rodlike, and wirelike structures (Figure S7). Figure 4a shows the dark-field optical image of the sample containing 6 μg/mL TMV in the absence of any polarizer. Then, we modified the setup, as shown in Figure 4b, such that the sample could be illuminated with right- and left-handed circularly polarized light, and optical rotation in the light scattered by the microwires could be detected. For this, a linear analyzer was added in the path of scattered light. Figure 4c shows changes in the average grayscale intensity for one of the microwires (inset, Figure 4c) upon alternate illumination with RCP and LCP light. This plot shows repeatability of the measurements as well as reveals that upon changing the illumination from LCP to RCP, the scattering intensity passing through the analyzer is reduced to 65%. Such an alteration of intensity proves that the individual microwires are chiral, as expected from their twisted structures. Quantification of the chirality of microwires was based on the optical rotation of scattered light. Precisely, to illuminate the sample with linearly polarized light at different angles, we kept a linear polarizer at the bottom of the sample (down-side polarizer, i.e., DPOL). Then, dark-field images were collected without and with analyzer, i.e., another linear polarizer kept above the sample (top-side polarizer, i.e., TPOL). These data are shown in Figure 4d,e, respectively. Then, the percentage reduction in scattering intensity (65%) due to the optical rotation was correlated with the changes in the linearly polarized scattering intensity upon varying angle of linearly polarized illumination. It showed that when illumination is changed from LCP to RCP, the scattered light rotates by 50°, which is a measurement of the optical rotation exhibited by the corresponding microwire. Notably, in aqueous dispersion, differential absorption for RCP and LCP was observed, but not optical rotation, as the TMV-AuNR$^+$ wires were oriented in all possible directions. Hence, output could be only circular and unpolarized light, and thus, bulk circular dichroism spectra were not affected by linear dichroism components.

Generalization of the Strategy Using Cellulose Nanocrystals (CNC). To show the generic nature of this approach, we used anisotropic nanocellulose particles, viz., CNC. Cellulose is found in many skeletal systems of plants, mostly in a chiral nematic liquid crystal phase. Below a critical concentration, a form of cellulose exists as a whisker-like colloidal substance[67] with an average aspect ratio of 12, known as CNC, whose cryo-TEM images are shown in Figure 5a. These rodlike CNCs contain sulfate half-ester groups on their surface and have a right-handed twisted structure,[68] which results in a helical distribution of negative surface charge similar to that of TMVs. Though these are not atomically precise, they are highly crystalline, the surface contains negatively charged groups (ζ-potential, −64 mV), and most importantly, these are produced cost-effectively from renewable resources. Earlier, CNCs have shown the potential to serve as a chiral template both in its nematic phase[69] and as single crystals.[70] Here, we added 0.02 wt % of colloidal CNC at each step to 0.16 nM AuNR$^+$ solution following the same strategy. As depicted in Figure 5b, the AuNR$^+$s attached to the CNC surface keeping their longitudinal axis parallel to that of the CNCs.

https://dx.doi.org/10.1021/acs.jpcc.0c11512
J. Phys. Chem. C 2021, 125, 3256−3267

Notably, in this case, they attached to the CNCs covering their entire surface. During the process, the positive ζ-potential of the system decreased continuously (Figure S8), suggesting surface charge neutralization through electrostatic assembly. Figure 5c shows that the absorption spectra gradually shift toward the right and get broadened, verifying a similar interaction as expected from the TMV case. Indeed, the TEM image of the sample at a low CNC concentration (Figure 5d) suggests that the $AuNR^+$s arranged themselves unidirectionally along the length of the CNC. At a higher concentration of CNC, a long-range assembly produced longer and thicker composite structures. In Figure 5e, we see such an assembled structure, where, although the CNCs are hardly visible due to low contrast, the pattern of $AuNR^+$ arrangement clearly indicates that they were longitudinally attached to an anisotropic soft template of higher aspect ratio. Circular dichroism study shows that CNC-$AuNR^+$ also produced a chiral signal at the position of the maximum absorption of $AuNR^+$. Similar to the case of TMV, with the increase in the concentration of CNC, as the microstructures grew, the system showed a stronger chiral signal keeping the zero-crossing position fixed. In the case of CNC, the template was not perfectly cylindrical like TMV, but they rather contained right-handed structural twist in their inherent geometry. Therefore, the CNC-$AuNR^+$ composite did not produce ribbon-like ordered structure with global twists. Instead, the nanorods evenly covered the CNC surfaces, guided by the grooves of CNCs. Several studies have shown that the dihedral angle between nanoparticles significantly alters their chiral response.[71] Although less ordered, the CNC-$AuNR^+$ assemblies contained higher relative angle between consecutive gold nanorods compared to their uniaxial end-to-end arrangement in the TMV-$AuNR^+$ system, which gave rise to a stronger CD signal in the case of CNC-$AuNR^+$.

The calculated g-factor of CNC-$AuNR^+$ implies that the chiral response of this system is comparable to that of TMV-$AuNR^+$ (Figure S9). Notably, the spectra fail to show a stronger signal intensity with an increase in CNC concentration beyond 0.06 wt % CNC. This can be attributed to the fact that CNC-templated assemblies of $AuNR^+$ show greater polydispersity, leading to a flattening of the absorbance spectra (as evident from Figure 5c). However, the strong CD spectra and standard g-factor values imply that our strategy works well for CNC too, which may be extended to any template of this kind.

CONCLUSIONS

In the field of template-assisted plasmonic chirality, we present a simple strategy to obtain a binary assembly with structural precision. Using surface chemistry as a key, by a slow stepwise addition of the rod-shaped chiral templates to a large pool of well-dispersed AuNRs, we observed systematic attachment of the AuNRs to the templates following their structural helicity. With a gradual increase in the template concentration in the system, these unit composite structures participate in a long-range assembly that gives longer, thicker wirelike structures with an overall structural chirality. Thus, by following the proper mixing protocol, without any sophisticated template or complex sample preparation technique or highly specialized and tedious chemical synthesis, we can create structures that show plasmonic chirality in the NIR wavelength region. Besides being simple and general in nature, this method is highly reproducible, easily scalable, and efficient for tuning the length of the structures (Figure 2c–e), thereby bridging between nanoscale and microscale structural chirality. Interestingly, although both TMV and CNC-templated assemblies of $AuNR^+$ give rise to plasmonic chirality around the same wavelength following the same strategy, they may be suitable for very different applications. If the radiative and nonradiative losses can be minimized, then the chiral plasmonic wires with length of several microns made of TMV-$AuNR^+$ might have potential utility in nonlinear optics and in telecommunication kind of devices. They can also be excellent waveguides to preferentially propagate one circularly polarized light over the other, due to their chirality. On the other hand, the CNC-$AuNR^+$ system does not give such long unidirectional structures, but at gradually higher concentration of CNC, they show increasingly stronger signal in CD spectra (Figure 5f). Hence, the CNC-$AuNR^+$ system would be more suitable for other applications where a strong chirality in the NIR region is crucial. Further, using PDFSMS, we could detect the chirality of a single TMV-$AuNR^+$ composite microwire. This method has the potential to detect TMV or similar chiral templates with an unprecedented detection limit. Thus, the chiral plasmonic materials proposed in this study hold importance to diverse fields of physics, chemistry, material science, and biology.

ASSOCIATED CONTENT

Supporting Information

The Supporting Information is available free of charge at https://pubs.acs.org/doi/10.1021/acs.jpcc.0c11512.

Additional characterization of AuNR before and after MUTAB functionalization; TEM images of TMV-$AuNR^+$ in the presence of low TMV concentration; scanning electron micrograph; polarized optical image and dark-field optical images of TMV-$AuNR^+$; cryo-TEM images of TMV-$AuNR^+$ resulting from reverse addition; raw circular dichroism spectra of TMV-$AuNR^+$ at various TMV concentrations; and change in ζ-potential of CNC-$AuNR^+$ system with increasing CNC concentration (PDF)

Tomographic reconstruction of $AuNR^+$ (AVI)

Tomographic reconstruction of TMV-$AuNR^+$ (AVI)

AUTHOR INFORMATION

Corresponding Authors

Mauri A. Kostiainen − *Department of Bioproducts and Biosystems, Aalto University, FI-00076 Aalto, Finland;* orcid.org/0000-0002-8282-2379; Email: mauri.kostiainen@aalto.fi

Robin H. A. Ras − *Department of Applied Physics and Department of Bioproducts and Biosystems, Aalto University, FI-00076 Aalto, Finland;* orcid.org/0000-0002-2076-242X; Email: robin.ras@aalto.fi

Thalappil Pradeep − *DST Unit of Nanoscience and Thematic Unit of Excellence, Department of Chemistry, Indian Institute of Technology Madras, Chennai 600036, India;* orcid.org/0000-0003-3174-534X; Email: pradeep@iitm.ac.in

Authors

Amrita Chakraborty − *DST Unit of Nanoscience and Thematic Unit of Excellence, Department of Chemistry,*

https://dx.doi.org/10.1021/acs.jpcc.0c11512
J. Phys. Chem. C 2021, 125, 3256−3267

Indian Institute of Technology Madras, Chennai 600036, India

Nonappa − *Faculty of Engineering and Natural Sciences, Tampere University, FI-33101 Tampere, Finland; Department of Applied Physics, Aalto University, FI-00076 Aalto, Finland;* orcid.org/0000-0002-6804-4128

Biswajit Mondal − *DST Unit of Nanoscience and Thematic Unit of Excellence, Department of Chemistry, Indian Institute of Technology Madras, Chennai 600036, India*

Kamalesh Chaudhari − *DST Unit of Nanoscience and Thematic Unit of Excellence, Department of Chemistry, Indian Institute of Technology Madras, Chennai 600036, India*

Heikki Rekola − *Institute of Photonics, University of Eastern Finland, FI-80101 Joensuu, Finland; Faculty of Engineering and Natural Sciences, Tampere University, FI-33101 Tampere, Finland;* orcid.org/0000-0003-3059-4535

Ville Hynninen − *Department of Applied Physics, Aalto University, FI-00076 Aalto, Finland*

Complete contact information is available at: https://pubs.acs.org/10.1021/acs.jpcc.0c11512

Author Contributions

A.C., T.P., M.A.K., and R.H.A.R. conceived the experimental design. A.C. prepared the samples and performed UV−vis studies and CD spectroscopy. N. performed cryo-TEM sample preparation and imaging, electron tomography reconstruction, and image analysis. B.M. collected TEM images. K.C. performed the PDFSMS study. H.R. carried out theoretical modeling of the CD spectrum. V.H. synthesized the CNCs. A.C. and N. wrote the first draft of the manuscript, and the final version of the manuscript was prepared through the contributions of all authors.

Notes

The authors declare no competing financial interest.

■ ACKNOWLEDGMENTS

The authors thank the Department of Science and Technology, Government of India, and the Academy of Finland (Project 308578), HYBER Centre of Excellence Programme (2014−2019), and Photonics Research and Innovation (PREIN, project no. 320166) flagship for supporting our research. A.C. and B.M. thank the Council of Scientific and Industrial Research and IIT Madras, respectively, for their research fellowships. The authors acknowledge the provision of facilities and technical support by Aalto University at OtaNano-Nanomicroscopy Center (Aalto-NMC). They also thank Prof. Anton Kuzyk and Ryssy Joonas for their support in circular dichroism measurements.

■ REFERENCES

(1) Blackmond, D. G. The origin of biological homochirality. *Cold Spring Harbor Perspect. Biol.* **2010**, *2*, No. a002147.

(2) Runnels, C. M.; Lanier, K. A.; Williams, J. K.; Bowman, J. C.; Petrov, A. S.; Hud, N. V.; Williams, L. D. Folding, Assembly, and Persistence: The Essential Nature and Origins of Biopolymers. *J. Mol. Evol.* **2018**, *86*, 598−610.

(3) Ranjbar, B.; Gill, P. Circular Dichroism Techniques: Biomolecular and Nanostructural Analyses- A Review. *Chem. Biol. Drug Des.* **2009**, *74*, 101−120.

(4) Nakanishi, K.; Berova, N.; Woody, R. *Circular Dichroism: Principles and Applications*; VCH: New York, 1994; p 230.

(5) Kelly, S. M.; Jess, T. J.; Price, N. C. How to study proteins by circular dichroism. *Biochim. Biophys. Acta, Proteins Proteomics* **2005**, *1751*, 119−139.

(6) Palmans, A. R. A.; Meijer, E. W. Amplification of Chirality in Dynamic Supramolecular Aggregates. *Angew. Chem., Int. Ed.* **2007**, *46*, 8948−8968.

(7) Liu, M.; Zhang, L.; Wang, T. Supramolecular Chirality in Self-Assembled Systems. *Chem. Rev.* **2015**, *115*, 7304−7397.

(8) Govorov, A. O. Plasmon-Induced Circular Dichroism of a Chiral Molecule in the Vicinity of Metal Nanocrystals. Application to Various Geometries. *J. Phys. Chem. C* **2011**, *115*, 7914−7923.

(9) Ben-Moshe, A.; Maoz, B. M.; Govorov, A. O.; Markovich, G. Chirality and chiroptical effects in inorganic nanocrystal systems with plasmon and exciton resonances. *Chem. Soc. Rev.* **2013**, *42*, 7028−7041.

(10) Oh, H. S.; Liu, S.; Jee, H.; Baev, A.; Swihart, M. T.; Prasad, P. N. Chiral Poly(fluorene-alt-benzothiadiazole) (PFBT) and Nanocomposites with Gold Nanoparticles: Plasmonically and Structurally Enhanced Chirality. *J. Am. Chem. Soc.* **2010**, *132*, 17346−17348.

(11) Hentschel, M.; Schaeferling, M.; Duan, X.; Giessen, H.; Liu, N. Chiral plasmonics. *Sci. Adv.* **2017**, *3*, No. e1602735.

(12) Lieberman, I.; Shemer, G.; Fried, T.; Kosower, E. M.; Markovich, G. Plasmon-Resonance-Enhanced Absorption and Circular Dichroism. *Angew. Chem., Int. Ed.* **2008**, *47*, 4855−4857.

(13) Wang, Y.; Xu, J.; Wang, Y.; Chen, H. Emerging chirality in nanoscience. *Chem. Soc. Rev.* **2013**, *42*, 2930−2962.

(14) Gansel, J. K.; Thiel, M.; Rill, M. S.; Decker, M.; Bade, K.; Saile, V.; von Freymann, G.; Linden, S.; Wegener, M. Gold Helix Photonic Metamaterial as Broadband Circular Polarizer. *Science* **2009**, *325*, 1513.

(15) Hodgkinson, I.; Wu, Q. H. Inorganic Chiral Optical Materials. *Adv. Mater.* **2001**, *13*, 889−897.

(16) Hendry, E.; Carpy, T.; Johnston, J.; Popland, M.; Mikhaylovskiy, R. V.; Lapthorn, A. J.; Kelly, S. M.; Barron, L. D.; Gadegaard, N.; Kadodwala, M. Ultrasensitive detection and characterization of biomolecules using superchiral fields. *Nat. Nanotechnol.* **2010**, *5*, 783−787.

(17) Tang, Y.; Cohen, A. E. Enhanced Enantioselectivity in Excitation of Chiral Molecules by Superchiral Light. *Science* **2011**, *332*, 333.

(18) Shukla, N.; Bartel, M. A.; Gellman, A. J. Enantioselective Separation on Chiral Au Nanoparticles. *J. Am. Chem. Soc.* **2010**, *132*, 8575−8580.

(19) Slocik, J. M.; Govorov, A. O.; Naik, R. R. Plasmonic Circular Dichroism of Peptide-Functionalized Gold Nanoparticles. *Nano Lett.* **2011**, *11*, 701−705.

(20) Shemer, G.; Krichevski, O.; Markovich, G.; Molotsky, T.; Lubitz, I.; Kotlyar, A. B. Chirality of Silver Nanoparticles Synthesized on DNA. *J. Am. Chem. Soc.* **2006**, *128*, 11006−11007.

(21) Govorov, A. O.; Gun'ko, Y. K.; Slocik, J. M.; Gérard, V. A.; Fan, Z.; Naik, R. R. Chiral nanoparticle assemblies: circular dichroism, plasmonic interactions, and exciton effects. *J. Mater. Chem.* **2011**, *21*, 16806−16818.

(22) García-Etxarri, A.; Dionne, J. A. Surface-enhanced circular dichroism spectroscopy mediated by nonchiral nanoantennas. *Phys. Rev. B* **2013**, *87*, No. 235409.

(23) Maoz, B. M.; Chaikin, Y.; Tesler, A. B.; Bar Elli, O.; Fan, Z.; Govorov, A. O.; Markovich, G. Amplification of Chiroptical Activity of Chiral Biomolecules by Surface Plasmons. *Nano Lett.* **2013**, *13*, 1203−1209.

(24) Merg, A. D.; Boatz, J. C.; Mandal, A.; Zhao, G.; Mokashi-Punekar, S.; Liu, C.; Wang, X.; Zhang, P.; van der Wel, P. C. A.; Rosi, N. L. Peptide-Directed Assembly of Single-Helical Gold Nanoparticle Superstructures Exhibiting Intense Chiroptical Activity. *J. Am. Chem. Soc.* **2016**, *138*, 13655−13663.

(25) Pigliacelli, C.; Sanjeeva, K. B.; Nonappa; Pizzi, A.; Gori, A.; Bombelli, F. B.; Metrangolo, P. In Situ Generation of Chiroptically-Active Gold-Peptide Superstructures Promoted by Iodination. *ACS Nano* **2019**, *13*, 2158−2166.

(26) Querejeta-Fernández, A.; Chauve, G.; Methot, M.; Bouchard, J.; Kumacheva, E. Chiral Plasmonic Films Formed by Gold Nanorods and Cellulose Nanocrystals. *J. Am. Chem. Soc.* **2014**, *136*, 4788−4793.
(27) Guerrero-Martínez, A.; Auguié, B.; Alonso-Gómez, J. L.; Džolić, Z.; Gómez-Graña, S.; Žinić, M.; Cid, M. M.; Liz-Marzán, L. M. Intense Optical Activity from Three-Dimensional Chiral Ordering of Plasmonic Nanoantennas. *Angew. Chem., Int. Ed.* **2011**, *50*, 5499−5503.
(28) Chen, L.; Zheng, J.; Feng, J.; Qian, Q.; Zhou, Y. Reversible modulation of plasmonic chiral signals of achiral gold nanorods using a chiral supramolecular template. *Chem. Commun.* **2019**, *55*, 11378−11381.
(29) Funck, T.; Nicoli, F.; Kuzyk, A.; Liedl, T. Sensing Picomolar Concentrations of RNA Using Switchable Plasmonic Chirality. *Angew. Chem., Int. Ed.* **2018**, *57*, 13495−13498.
(30) Kuzyk, A.; Schreiber, R.; Fan, Z.; Pardatscher, G.; Roller, E.-M.; Högele, A.; Simmel, F. C.; Govorov, A. O.; Liedl, T. DNA-based self-assembly of chiral plasmonic nanostructures with tailored optical response. *Nature* **2012**, *483*, 311−314.
(31) Zhou, C.; Duan, X.; Liu, N. DNA-Nanotechnology-Enabled Chiral Plasmonics: From Static to Dynamic. *Acc. Chem. Res.* **2017**, *50*, 2906−2914.
(32) Feng, W.; Kadiyala, U.; Yan, J.; Wang, Y.; DiRita, V. J.; VanEpps, J. S.; Kotov, N. A. Plasmonic nanoparticles assemblies templated by helical bacteria and resulting optical activity. *Chirality* **2020**, *32*, 899−906.
(33) Selivanovitch, E.; Douglas, T. Virus capsid assembly across different length scales inspire the development of virus-based biomaterials. *Curr. Opin. Virol.* **2019**, *36*, 38−46.
(34) Sasaki, E.; Hilvert, D. Self-Assembly of Proteinaceous Multishell Structures Mediated by a Supercharged Protein. *J. Phys. Chem. B* **2016**, *120*, 6089−6095.
(35) Kostiainen, M. A.; Hiekkataipale, P.; Laiho, A.; Lemieux, V.; Seitsonen, J.; Ruokolainen, J.; Ceci, P. Electrostatic assembly of binary nanoparticle superlattices using protein cages. *Nat. Nanotechnol.* **2013**, *8*, 52−56.
(36) Fraenkel-Conrat, H. Tobacco Mosaic Virus. In *The History of Tobacco Mosaic Virus and the evolution of Molecular Biology*; Plenum: New York, 1986; pp 5−17.
(37) Feng, W.; Kim, J.-Y.; Wang, X.; Calcaterra, H. A.; Qu, Z.; Meshi, L.; Kotov, N. A. Assembly of mesoscale helices with near-unity enantiomeric excess and light-matter interactions for chiral semiconductors. *Sci. Adv.* **2017**, *3*, No. e1601159.
(38) Chapman, S. N. *Plant Virology Protocols: From Viral Sequence to Protein Function*, 2nd ed.; Humana Press Inc.: NJ, 2008; p 677.
(39) Liljeström, V.; Ora, A.; Hassinen, J.; Rekola, H.; Nonappa; Heilala, M.; Hynninen, V.; Joensuu, J.; Ras, R.; Törmä, P.; Ikkala, O.; Kostiainen, M. Cooperative colloidal self-assembly of metal-protein superlattice wires. *Nat. Commun.* **2017**, *8*, No. 671.
(40) Samal, A.; Sreenivasan, S.; Thalappil, P. Investigation of the role of NaBH4 in the chemical synthesis of gold nanorods. *J. Nanopart. Res.* **2010**, *12*, 1777−1786.
(41) Hynninen, V.; Hietala, S.; McKee, J. R.; Murtomäki, L.; Rojas, O. J.; Ikkala, O.; Nonappa. Inverse Thermoreversible Mechanical Stiffening and Birefringence in a Methylcellulose/Cellulose Nanocrystal Hydrogel. *Biomacromolecules* **2018**, *19*, 2795−2804.
(42) Mastronarde, D. N. SerialEM: A Program for Automated Tilt Series Acquisition on Tecnai Microscopes Using Prediction of Specimen Position. *Microsc. Microanal.* **2003**, *9*, 1182−1183.
(43) Mastronarde, D. N. Automated electron microscope tomography using robust prediction of specimen movements. *J. Struct. Biol.* **2005**, *152*, 36−51.
(44) Nonappa, N.; Engelhardt, P. Electron Tomography of Whole Mounts. *Imaging Microsc.* **2019**, *21*, 22−24.
(45) Kremer, J. R.; Mastronarde, D. N.; McIntosh, J. R. Computer Visualization of Three-Dimensional Image Data Using IMOD. *J. Struct. Biol.* **1996**, *116*, 71−76.
(46) Engelhardt, P. Three-dimensional reconstruction of chromosomes using electron tomography. *Methods Mol. Biol.* **2007**, *369*, 365−385.
(47) Yang, W. H.; Schatz, G. C.; Van Duyne, R. P. Discrete dipole approximation for calculating extinction and Raman intensities for small particles with arbitrary shapes. *J. Chem. Phys.* **1995**, *103*, 869−875.
(48) García de Abajo, F. J. Colloquium: Light scattering by particle and hole arrays. *Rev. Mod. Phys.* **2007**, *79*, 1267−1290.
(49) Moroz, A. Depolarization field of spheroidal particles. *J. Opt. Soc. Am. B* **2009**, *26*, 517−527.
(50) Bohren, C. F.; Huffman, D. R. *Absorption and Scattering of Light by Small Particles*; John Wiley and Sons: NJ, 1983; p 530.
(51) Lin, R. D.; Steinmetz, N. F. Tobacco mosaic virus delivery of mitoxantrone for cancer therapy. *Nanoscale* **2018**, *10*, 16307−16313.
(52) Anaya-Plaza, E.; Aljarilla, A.; Beaune, G.; Nonappa; Timonen, J. V. I.; de la Escosura, A.; Torres, T.; Kostiainen, M. A. Phthalocyanine−Virus Nanofibers as Heterogeneous Catalysts for Continuous-Flow Photo-Oxidation Processes. *Adv. Mater.* **2019**, *31*, No. 1902582.
(53) Zhang, J.; Zhou, K.; Zhang, Y.; Du, M.; Wang, Q. Precise Self-Assembly of Nanoparticles into Ordered Nanoarchitectures Directed by Tobacco Mosaic Virus Coat Protein. *Adv. Mater.* **2019**, *31*, No. 1901485.
(54) Dujardin, E.; Peet, C.; Stubbs, G.; Culver, J.; Mann, S. Organization of Metallic Nanoparticles Using Tobacco Mosaic Virus Templates. *Nano Lett.* **2003**, *3*, 413−417.
(55) Czapar, A. E.; Zheng, Y.-R.; Riddell, I. A.; Shukla, S.; Awuah, S. G.; Lippard, S. J.; Steinmetz, N. F. Tobacco Mosaic Virus Delivery of Phenanthriplatin for Cancer therapy. *ACS Nano* **2016**, *10*, 4119−4126.
(56) Sánchez-Iglesias, A.; Grzelczak, M.; Pérez-Juste, J.; Liz-Marzán, L. M. Binary Self-Assembly of Gold Nanowires with Nanospheres and Nanorods. *Angew. Chem., Int. Ed.* **2010**, *49*, 9985−9989.
(57) Correa-Duarte, M. A.; Pérez-Juste, J.; Sánchez-Iglesias, A.; Giersig, M.; Liz-Marzán, L. M. Aligning Au Nanorods by Using Carbon Nanotubes as Templates. *Angew. Chem., Int. Ed.* **2005**, *44*, 4375−4378.
(58) Li, T.; Zan, X.; Winans, R. E.; Wang, Q.; Lee, B. Biomolecular Assembly of Thermoresponsive Superlattices of the Tobacco Mosaic Virus with Large Tunable Interparticle Distances. *Angew. Chem., Int. Ed.* **2013**, *52*, 6638−6642.
(59) Warmke, H. E.; Edwardson, J. R. Electron microscopy of crystalline inclusions of tobacco mosaic virus in leaf tissue. *Virology* **1966**, *30*, 45−57.
(60) Niu, Z.; Bruckman, M.; Kotakadi, V. S.; He, J.; Emrick, T.; Russell, T. P.; Yang, L.; Wang, Q. Study and characterization of tobacco mosaic virus head-to-tail assembly assisted by aniline polymerization. *Chem. Commun.* **2006**, 3019−3021.
(61) Gibaud, T.; Barry, E.; Zakhary, M. J.; Henglin, M.; Ward, A.; Yang, Y.; Berciu, C.; Oldenbourg, R.; Hagan, M. F.; Nicastro, D.; Meyer, R. B.; Dogic, Z. Reconfigurable self-assembly through chiral control of interfacial tension. *Nature* **2012**, *481*, 348−351.
(62) Yeom, J.; Yeom, B.; Chan, H.; Smith, K. W.; Dominguez-Medina, S.; Bahng, J. H.; Zhao, G.; Chang, W. S.; Chang, S. J.; Chuvilin, A.; Melnikau, D.; Rogach, A. L.; Zhang, P.; Link, S.; Král, P.; Kotov, N. A. Chiral templating of self-assembling nanostructures by circularly polarized light. *Nat. Mater.* **2015**, *14*, 66.
(63) Nguyen, L.; Dass, M.; Ober, M. F.; Besteiro, L. V.; Wang, Z. M.; Nickel, B.; Govorov, A. O.; Liedl, T.; Heuer-Jungemann, A. Chiral Assembly of Gold−Silver Core−Shell Plasmonic Nanorods on DNA Origami with Strong Optical Activity. *ACS Nano* **2020**, *14*, 7454−7461.
(64) Vinegrad, E.; Vestler, D.; Ben-Moshe, A.; Barnea, A. R.; Markovich, G.; Cheshnovsky, O. Circular Dichroism of Single Particles. *ACS Photonics* **2018**, *5*, 2151−2159.
(65) Karst, J.; Cho, N. H.; Kim, H.; Lee, H.-E.; Nam, K. T.; Giessen, H.; Hentschel, M. Chiral Scatterometry on Chemically Synthesized Single Plasmonic Nanoparticles. *ACS Nano* **2019**, *13*, 8659−8668.

https://dx.doi.org/10.1021/acs.jpcc.0c11512
J. Phys. Chem. C 2021, 125, 3256−3267

(66) Chaudhari, K.; Pradeep, T. Optical rotation by plasmonic circular dichroism of isolated gold nanorod aggregates. *Appl. Phys. Lett.* **2014**, *105*, No. 203105.
(67) Kontturi, E.; Laaksonen, P.; Linder, M. B.; Nonappa; Gröschel, A. H.; Rojas, O. J.; Ikkala, O. Advanced Materials through Assembly of Nanocelluloses. *Adv. Mater.* **2018**, *30*, No. 1703779.
(68) Usov, I.; Nyström, G.; Adamcik, J.; Handschin, S.; Schütz, C.; Fall, A.; Bergström, L.; Mezzenga, R. Understanding nanocellulose chirality and structure−properties relationship at the single fibril level. *Nat. Commun.* **2015**, *6*, No. 7564.
(69) Cheng, Z.; Ma, Y.; Yang, L.; Cheng, F.; Huang, Z.; Natan, A.; Li, H.; Chen, Y.; Cao, D.; Huang, Z.; Wang, Y.; Liu, Y.; Yang, R.; Zhu, H. Plasmonic-Enhanced Cholesteric Films: Coassembling Anisotropic Gold Nanorods with Cellulose Nanocrystals. *Adv. Opt. Mater.* **2019**, *7*, No. 1801816.
(70) Majoinen, J.; Hassinen, J.; Haataja, J. S.; Rekola, H. T.; Kontturi, E.; Kostiainen, M. A.; Ras, R. H. A.; Törmä, P.; Ikkala, O. Chiral Plasmonics Using Twisting along Cellulose Nanocrystals as a Template for Gold Nanoparticles. *Adv. Mater.* **2016**, *28*, 5262−5267.
(71) Kuzyk, A.; Schreiber, R.; Zhang, H.; Govorov, A. O.; Liedl, T.; Liu, N. Reconfigurable 3D plasmonic metamolecules. *Nat. Mater.* **2014**, *13*, 862−866.

https://dx.doi.org/10.1021/acs.jpcc.0c11512
J. Phys. Chem. C 2021, 125, 3256−3267